Wetting and adhesion of a polymer melt on porous self-assembled polymer substrates by breath figure templating

Pierre Escalé, Cédric Giraudet, Maud Save, Laurent Billon, Ross Brown, Christophe Derail, Laurent Rubatat

Macromolecular Chemistry and Physics
www.mcp-journal.de

Wetting and Adhesion of a Polymer Melt on Porous Self-Assembled Polymer Substrates by Breath Figure Templating

*Cédric Giraudet, Pierre Escalé, Maud Save, Laurent Billon, Ross Brown, Christophe Derail, and Laurent Rubatat**

This study addresses the wetting and adhesion of a low molecular mass poly(*n*-butyl acrylate) homopolymer melt, used as a weak acrylic adhesive, on two types of textured polymer films prepared by the breath figure templating method. The first film is a polystyrene homopolymer honeycomb-like structure with well-defined porous structure and long-range ordering. The second is a disordered poly(*n*-butyl acrylate)-*block*-polystyrene diblock copolymer film featuring a broad distribution of pore diameters. Static contact angle measurements show that porous films repel better the polymer melt than the corresponding nontextured films. Contact angles and spreading of polymer melt droplets on these textured surfaces reveals a Cassie-Baxter state on the ordered porous film and a partial Wenzel state on the disordered porous films. In addition, probe tack results show that the textured surfaces tend to induce cavitation. The correlation between the wetting and adhesion highlights the major role of melt insertion into the pores, which is primarily controlled by the pores' dimensions.

1. Introduction

Since its introduction in 1994 by François et al.,[1] the preparation of ordered porous polymer films, so-called honeycomb (HC) films, by the breath figure (BF) method has received considerable interest. Indeed, the BF approach is a rapid, inexpensive, and robust route to build-up HC films.[2–6] Recently, high-quality HC films, up to 20×20 cm^2 were manufactured, opening transfer of these promising lab-materials to several technological applications.[7,8] The BF process occurs when the vapor of a solute, e.g., water, condenses in droplets on an evaporating polymer solution, leading to imprints, i.e., pores, in the polymer film after complete evaporation of the solute.[1,9,10] The simplicity of HC pattern-formation led to the preparation of hierarchically ordered porous films using a wide variety of polymers,[2,3,5] including coil–coil,[5,11–13] rod-coil,[14] hybrid,[15,16] or biohydrid[17] block copolymers. Hierarchy in the porosity was also described using a sacrificial block[18] or using a water/ethanol atmosphere.[19] BF films were used to prepare hydrophobic and super hydrophobic biomimetic surfaces, which can sense pH,[11] temperature,[20] or CO_2.[21,22] Then, many targeted potential applications[3] are related to formation of an interface between the porous surface and cell,[23–25] bacteria,[26,27] liquid crystal,[28] or Newtonian liquid.[29–32] With that respect, water adhesion was intensively studied on BF films varying porosity and/or surface chemistry mainly via contact angle (CA),[29–31] and more seldom on droplets via microbalance measurements.[32] Indeed, the microbalance setup allows to effectively measure droplet adhesion forces, which can be tuned by varying the pore internal negative pressures via their diameter.[32] It is worth to note that adhesive tapes were already used to peel off the top layer of HC films to create micropillared structured surface.[11,33,34] This is pointing out the polymeric substrate fragility when tough adhesives are used.

From the adhesion and wetting perspectives, controlled polymer surface-patterning is widely employed in studies of the surface wettability[35,36] or the adhesion for pressure sensitive adhesion (PSA).[37–39] The role of the substrate texture in adhesion was mainly studied by peeling or JKR tests (by Johnson, Kendall, and Roberts) on model surfaces with different patterning.[40,41] Furthermore, the rheological properties of adhesives[42–45] and substrates[38,40,46–48] play an important role in deformation and energy dissipation during peeling or probe tack tests.[49] Probe tack studies have been broadly performed on smooth substrates (i.e., nontextured) with adhesives,[50,51] so as Newtonian liquids for which the tacking kinetics is driven by a cavitation and, then, fingering regimes.[52,53] Nevertheless, in the literature, there are few reports on probe tack experiments dedicated to Newtonian

C. Giraudet[+], P. Escalé[++], M. Save, L. Billon, R. Brown, C. Derail, L. Rubatat
Universite de Pau et des Pays de l'Adour
E2S UPPA, CNRS, IPREM, Pau France
E-mail: laurent.rubatat@univ-pau.fr
L. Billon
Bio-inspired Materials group: Functionalities & Self-assembly
IPREM, Universite de Pau et des Pays de l'Adour
Pau, France

The ORCID identification number(s) for the author(s) of this article can be found under https://doi.org/10.1002/macp.202200273

[+]Present address: Universite de Pau et des Pays de l'Adour, E2S UPPA, CNRS, TotalEnergies, LFCR UMR5150, Anglet, France

[++]Present address: Arkema, Groupement de Recherche de Lacq, BP 34, 64170, Lacq, France

DOI: 10.1002/macp.202200273

Table 1. Characteristics of the polymers used in this study.

	PS	P*n*BA-*b*-PS	P*n*BA
M_w [g·mol^{-1}]	22 900	122 400	7600
$Đ$	1.19	1.37	1.23
Wt% of P*n*BA	–	62	–

liquids on top of porous substrates. Jah and Tirumkudulu modelized squeezed Newtonian liquids on surfaces with few-micron-sized pores that agree with experimental data collected on porous alumina substrates and silicon oils of various viscosities.[54] Interestingly, their model points out the impact of pores on the initiation of cavitation mechanism. This is matching results obtained with PSA highlighting that strong substrate-roughness hinders the nucleation of cavities at the interface and also slows down the growth of interfacial cracks.[55] Focusing on BF polymer substrates, only few studies report on adhesion force measurements, which are restricted to small droplets of oil[56] and water,[32] using a microbalance setups as already mentioned.

In the present work, we successfully measured adhesion forces and monitored probe tack regimes, over 50 mm^2, of a polymer melt on two different surface porosities regularly obtained through the BF method: (i) HC films with a long-range ordering obtained with a polystyrene (PS) homopolymer, and (ii) disordered porous films consisting of poly(*n*-butyl acrylate)-*block*-polystyrene diblock copolymer (P*n*BA-*b*-PS). PS homopolymer is selected for investigating the influence of pore ordering, since it is known to favor highly ordered HC film formation.[12] On the other hand, the use of the P*n*BA-*b*-PS copolymer allows to tune the chemical nature of the interface toward a higher affinity with the melt. In addition, the introduction of the PS block facilitates the BF process and brings mechanical strength via the microphase separation. Poly(*n*-butyl acrylate) (P*n*BA) homopolymer with low molar mass is chosen as polymer melt to allow wettability and adhesion forces measurements by static CA and probe tack tests, respectively, without damaging the substrate. Finally, the data are correlated to point out the specific role of pores' dimensions and surface-fluid chemical affinity on these properties.

2. Experimental Section

2.1. Polymers and Film Preparation

The characteristics of the polymers, i.e., weight-average molar mass M_w, dispersity $Đ$, and mass block ratio, measured by nuclear magnetic resonance and size exclusion chromatography are summarized in **Table 1**. Both polymers used in this study, namely the PS homopolymer and the P*n*BA-*b*-PS diblock copolymer, are synthesized by nitroxide-mediated polymerization using Blockbuilder as a controlling agent. The details on the copolymer synthesis is given in the reference.[12] Porous films were built-up by casting droplets of polymer solutions, at 5 g·L^{-1} in carbon disulfide, on glass substrates under a humid air flux (2 L·min^{-1}, relative humidity: 55–65%). In parallel, smooth films, i.e., without porosity, were prepared from the same stock solutions in absence of humidity air flow. The films are typically about 500 µm thick.

Table 1 presents the characteristics of the P*n*BA polymer used as adhesive fluid. Since the molar mass of the adhesive melt is significantly below the molar mass between entanglement of P*n*BA (M_e = 32 000 g·mol^{-1}), it behaves as a viscous liquid.[57] Its dynamic viscosity is 60 Pa·s^{-1}, as estimated using the model of Jullian et al.[57] In the present work, the molar mass of P*n*BA was chosen below M_e to allow reliable contact angle and probe tack measurements without damaging the weak polymer substrate morphologies. Prior to the experiments, the samples were degassed for several hours in a vacuum chamber.

2.2. Microscopy Techniques

Wet and dry porous samples are imaged at several length scales. Optical transmission images are collected on a Leica DM/LM microscope equipped with a Leica DFC280 camera using magnification factors of 20 and 50. Scanning electron microscopy (SEM) is performed on an IROX SH3000 microscope at 5 or 10 kV. The distributions of pore diameters are derived with ImageJ.[58] Atomic force microscopy (AFM) is performed with an Innova AFM (Veeco Instrument Inc.). AFM phase images are scanned in tapping mode under ambient conditions, using rectangular silicon cantilevers (MMP-12100-10, Veeco-probes) at a nominal resonance frequency of 150 kHz. The ratio of the real area to the projected area, *r*, is given by the Bruker NanoScope Analysis software.

2.3. Contact Angle Measurements

A 5 mm diameter drop of P*n*BA oligomer is deposited on top of the surfaces to measure the static CA at room temperature, i.e., about 20 °C. A TECLIS Tracker with a Telecentric 55 mm camera is used. Static CA's is derived from the images using Windrop 1.9 software.

2.4. Probe Tack Experiments

The setup used in this study, originally developed by Poivet et al.,[53] couples conventional tack measurements with in-situ observation using a fast camera (Baumer Inc.). Probe displacement and the force are collected at rates between 10 and 1000 Hz. The camera can collect up to 500 frames per second with a resolution of 100 µm. The load cell used in this study has a capacity of 50 N with an accuracy of 0.1 N (TMC). The rigidity of the apparatus is given at $(2.5 \pm 0.5) \times 10^5$ N·m^{-1}. The polymer melt is deposited on the coated glass substrates and a 8 mm diameter stainless-steel probe is pressed into contact, maintaining a compression force of 40 N for 200 s. We adjust the amount of deposited melt to generate a slight excess around the probe, guarantying a homogeneous layer of melt under the whole probe. Traction measurements are performed at room temperature with displacement velocities of 50 and 500 µm·s^{-1}. Extraction of the displacement, $h(t)$, and the force, $F(t)$, as function of time, t, is described in the reference.[52] The tack energy, needed to fully separate the probe from the substrate, is determined by integrating the force curve versus the displacement.

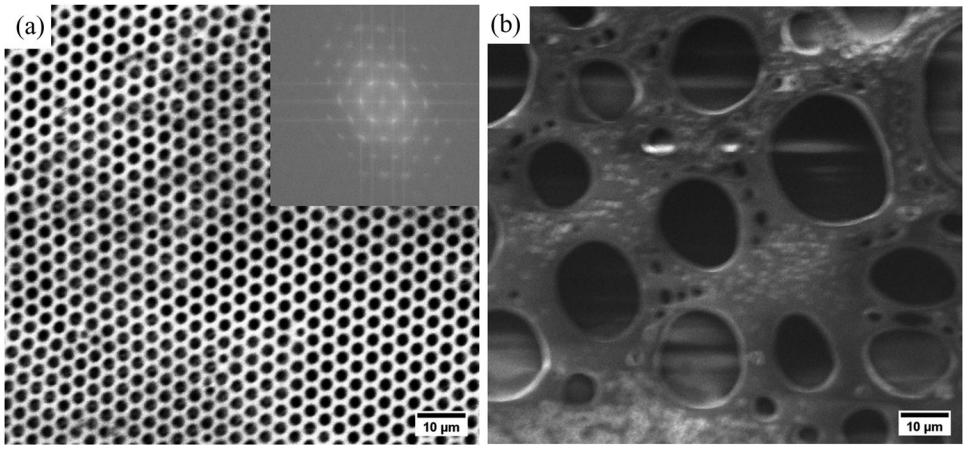

Figure 1. Contrasting long-range order and disordered of the PS and P*n*BA-*b*-PS porous films. a) SEM images of PS film (inset shows the Fourier transform of a ≈ 170 × 120 μm^2 area). b) Image of P*n*BA-*b*-PS film. Scale bars are 10 μm.

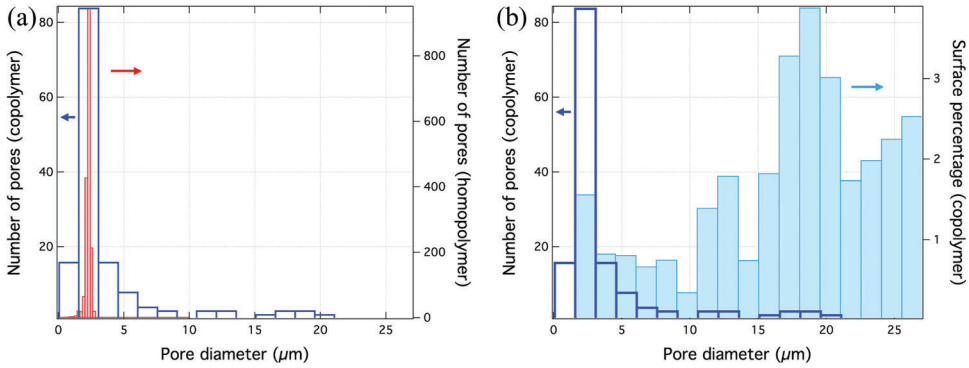

Figure 2. Contrasting pore size distribution of the ordered PS homopolymer and the disordered P*n*BA-*b*-PS copolymer films. a) Number distributions of pore diameter. Red shaded bars: PS pore distribution; blue open bars: copolymer. b) Contribution to surface area versus pore diameter. Blue shaded bars: P*n*BA-*b*-PS copolymer film; blue open bars: for comparison, pore number distribution for the copolymer.

3. Results

3.1. Surface Characterization of Porous Films

The SEM micrograph in **Figure 1**a shows the highly ordered HC structure of the PS homopolymer porous film. The Fourier transform in the inset of about 170 × 120 μm^2 region, illustrates the long-range hexagonal ordering. The average apparent pore diameter on the surface is 2.2 μm with a pore-to-pore averaged distance of 3.6 μm. The pore diameter distribution shown in **Figure 2**a is based on 1745 detected pores. It is sharp with a standard deviation of 0.25 μm. The analysis also yields the total exposed polymer surface fraction, which is 55% of the PS film surface.

Figure 1b shows a representative image of the P*n*BA-*b*-PS block copolymer porous films in the central region, where the CA and probe tack tests were performed. The porosity is highly disordered with a large dispersity of pore size. It should be mentioned that higher ordering is given in the outer part of the film as demonstrated in the reference.[12] The further away from the edge of the sample, the lower is the degree of ordering. The copolymer film pore distribution (Figure 2a), based on 153 detected pores, also peaks around 2 μm with a tail stretching to 26 μm. The distribution weighted by contribution to the total sample area (Figure 2b), shows the dominant contribution of large pores (>10 μm) to the surface porosity. The total exposed polymer surface fraction is 65% of the P*n*BA-*b*-PS film surface.

To complete the surface characterization, tapping mode AFM was performed to evaluate the ratio of the real area over the projected area, named *r*, (cf. Equation 1). The topographic images are presented in Figure S1 (Supporting Information). The *r* values on both porous films are 1.491 and 1.336 for PS and P*n*BA-*b*-PS, respectively. Detailed pore's depth profiles observation was not performed in the present study. However, it was done on a similar system in the reference,[13] where HC film cross-sections reveal quasispherical pores with circular openings on top of the film.

In addition to the micrometer porous structure, the use of the P*n*BA-*b*-PS block copolymer induces a microphase separation at the surface of the film, shown by AFM tapping mode phase images in **Figure 3**. The copolymer self-assembly appears with bright 50 nm dots in the darker matrix between the micrometer-sized pores. Considering the composition in Table 1, the bright dots are PS-rich domains while the matrix consists mainly of P*n*BA. The nanostructure is also confirmed in bulk by SAXS and SANS as presented in Figure S2 (Supporting Information).

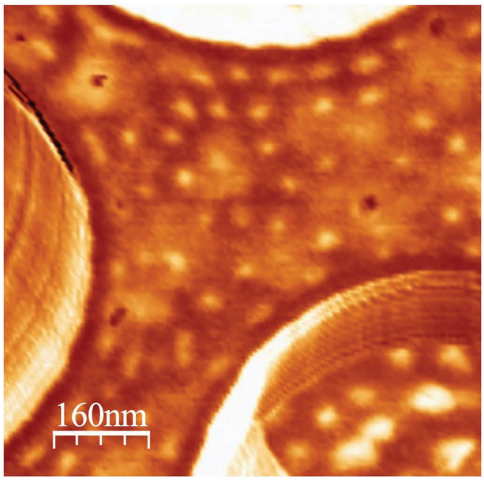

Figure 3. Microphase separation in the matrix around the pores of the P*n*BA-*b*-PS block copolymer. AFM tapping mode phase image.

Table 2. Static CA measured on smooth and BF films prepared with PS and P*n*BA-*b*-PS copolymers. Mean and standard deviation of five measurements.

	PS	P*n*BA-*b*-PS
Smooth films	23° ± 1°	19° ± 1°
Porous films	84° ± 1°	59° ± 1°

3.2. Static Contact Angle Measurements

CAs) give insight into the affinity of a low molar mass P*n*BA for smooth and porous films prepared from PS and P*n*BA-*b*-PS. Values in **Table 2** are the average of at least five independent measurements.

The static CAs on both smooth films are close but as expected, the CA measured on the P*n*BA-b-PS copolymer (62 wt% of P*n*BA) is lower than the pure PS because of a higher affinity with the P*n*BA polymer melt. Nevertheless, it can be noticed that the CA values on smooth PS films are relatively low for two highly immiscible polymers. On the other hand, CAs on the textured surfaces are significantly greater, possibly indicating Cassie-Baxter behavior arising from the porosity, i.e., the P*n*BA droplets are in contact with solid polymers and air is trapped in the pores.[59] However, intrusion of polymer melt in the pores, i.e., partial Wenzel mode, cannot be excluded. The theoretical condition of a transition between the Cassie-Baxter to Wenzel configuration is given by the following equation:[60,61]

$$\cos(\alpha_p) > (1 - \upsilon_p)/(r - \upsilon_p) \quad (1)$$

where α_p is the CA measured on the smooth films, r is the ratio of the real area to the projected area, and υ_p is the polymer fraction in contact with liquid drop. Although Equation 1 is satisfied with both PS and P*n*BA-*b*-PS experimental values, indicating that the liquid can penetrate inside the pores, a better representation of the interfacial behavior was proposed by Bormashenko et al.[62] Indeed, in the specific case of HC polymer films in which the liquid fully penetrate the porosity, they suggested to consider the liquid–liquid interface at the pore openings in the Cassie expression. Therefore, for full liquid intrusion in a fraction of pores, the overall CA on the BF porous surface α can be related to the CAs on smooth films (α_p) as well as between the liquid–air ($\alpha_a = 180°$) and liquid–liquid ($\alpha_L = 0°$) interfaces, by the relation:

$$\cos(\alpha) = \upsilon_p \cdot \cos(\alpha_p) + \upsilon_a \cdot \cos(\alpha_a) + \upsilon_L \cdot \cos(\alpha_L) \quad (2)$$

where υ_p, υ_a, and υ_L are fractional contributions of, respectively, the polymer matrix, empty pores, and pores filled of liquid; thus $\upsilon_p + \upsilon_a + \upsilon_L = 1$. Equation 2 can be then reduced to:

$$\cos(\alpha) = \upsilon_p \cdot (\cos(\alpha_p) + 1) + 2 \cdot \upsilon_L - 1 \quad (3)$$

Applying this equation to the experimental data allows to evaluate υ_L, which leads to 0.024 for the PS porous film and 0.125 for the P*n*BA-*b*-PS one. The first value can be neglected, meaning that the regular Cassi-Baxter mode with air–liquid interfaces in the pores openings agrees with the PS experimental observations. On the other hand, the P*n*BA-*b*-PS value clearly indicates that 12.5% of the total surface corresponds to pores filled with the polymer melt. This partial intrusion is favored by the presence of larger pores and an affinity of the fluid with the copolymer surface containing a P*n*BA majority phase. Assuming that the larger pores are filled first, a pore diameter threshold can be estimated from the υ_L value and from the pore surface distribution (Figure 2b). It can be then determined that, without applied pressure, pores smaller than about 20 µm remain empty.

3.3. Spreading Dynamics

The melt spreads very differently on the ordered and disordered porous films, see **Figure 4**. On the HC films (PS substrates), the droplet is pinned by the pores, leading to a segmented contact line complying to the hexagonal pattern of the substrate. As already reported by Bormashenko, the contact line cannot sit on or in half a pore.[63] The contact line advances slowly on average (see the pictures 2 min apart in Figure S4, Supporting Information). The melt behaves differently on the copolymer porous film with an evident spreading, see Figure S4 (Supporting Information). This faster spreading on the copolymer substrate might be favored by the presence of larger pores (>20 µm), more easily filled by the melt, contrary to the PS-based BF film with about ten-times smaller pores.

3.4. Probe Tack Experiments

As reported above, porous PS films show long-ranged ordering; on the other hand, P*n*BA-*b*-PS ones are ordered on the edges and erratic in the center. Therefore, to probe the overall adhesiveness of the melt on the substrates, we performed tack experiments with a large probe, i.e., 8 mm diameter, typically ten-times larger than microbalance-based methods where the probe is a droplet of the adhesive fluid itself.[32,56,64] In all cases, the substrates were not damaged after the experiments. **Figure 5** shows the force-distance curves recorded during the detachment of the P*n*BA melt deposited on smooth and BF surfaces prepared from

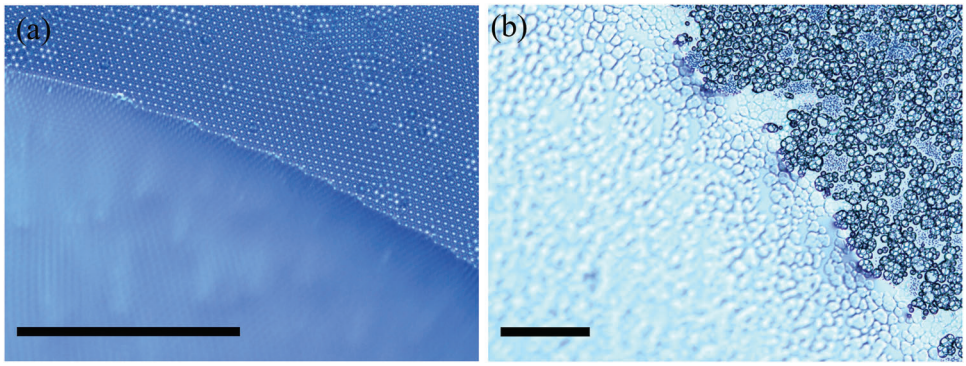

Figure 4. Optical transmission images taken at the edge of the polymer droplet (contact line) deposited on a PS (a, 50×) and a P*n*BA-*b*-PS (b, 20×) porous films. Scale bares: 100 µm.

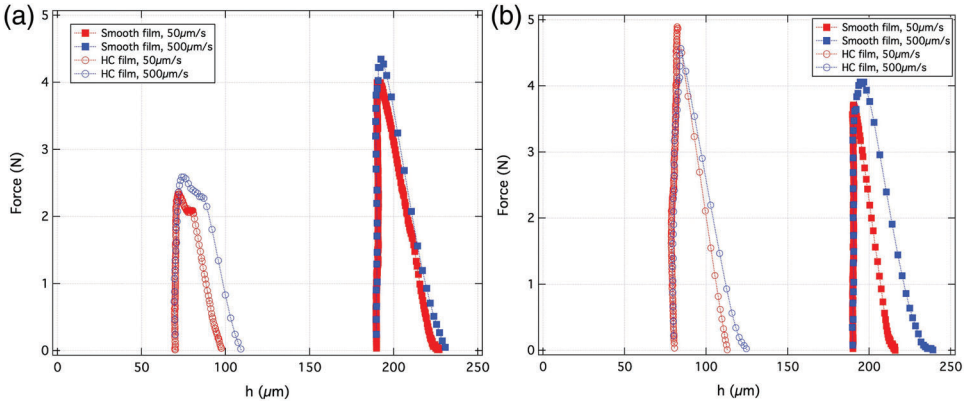

Figure 5. Tack experiments show cavitation on porous PS films and fingering on smooth films. a) PS films, b) P*n*BA-*b*-PS films. Solid symbols smooth films; open symbols, porous films. Traction force versus probe substrate separation (h) is shown at 50 (red) and 500 µm·s^{-1} (blue).

Table 3. Tack energy as a function of the probe traction velocity measured on four different substrates smooth or porous PS and copolymer films.

	PS		P*n*BA-*b*-PS	
Probe velocity [µm·s^{-1}]	50	500	50	500
Smooth film [J·m^{-2}]	2.0 ± 0.2	3.4 ± 0.3	2.2 ± 0.2	3.4 ± 0.3
Porous film [J·m^{-2}]	0.8 ± 0.2	1.6 ± 0.4	2.0 ± 0.5	2.9 ± 0.7

both polymers, after an initial compression of 40 N for 200 s. The preload compression largely increases the impregnation of the melt into the pores. This is reflected by the initial melt thickness after preload, h_0, which ranges between 150 and 200 µm for smooth films and only 50 and 100 µm for the HC films. **Table 3** reports the energies needed to fully separate the probe from the substrate. Variability of the tack energy is estimated to 10% on smooth films, related to slight tilt errors between the sample and probe surfaces, and of about 25% on the porous films. Greater variability on the porous films is attributed to surface texture fluctuations. Nevertheless, general trends emerge: the tack energy tends to increase with the traction speed and the values measured on the two smooth substrates are relatively close at both rates. Thus, the slight difference in chemical nature of both surfaces (PS vs P*n*BA-*b*-PS) does not seem to play a significant role in probe tack adhesion. On the other hand, tack energies on textured films are all lower than those measured on smooth films. This decrease can be related to a lower solid contact with the polymer melt, 55% and 65%, respectively, for the PS and P*n*BA-*b*-PS substrates measured by SEM. Note that the decrease is more pronounced for the PS films, in agreement with a significantly lower solid interface. From the analysis of the shape of the curves, one can see that the different tack regimes[52,53] are greatly influenced by the films texture. The tack curves for the PS substrates (Figure 5a) show a force plateau with the HC films, which can be associated with a cavitation regime and more specifically with the cavities longitudinal extension. On the other hand, the tack curves of smooth PS film indicate a pronounced fingering regime. For the P*n*BA-*b*-PS substrates (Figure 5b), the measured tack curves shape are similar for both porous and smooth films, suggesting principally fingering.

In-situ optical microscopy transmission images, with a 100 µm resolution, complement the tack measurements. Data are available only for the P*n*BA-*b*-PS copolymer substrates which remain transparent when textured, **Figure 6**; the µm-scale texture of the PS film scatters too strongly. Figure 6a unambiguously shows fingering regime on smooth film, in agreement with the probe tack curves. On the other hand, images collected on the porous film (Figure 6b) show a slight fingering process limited to the edge

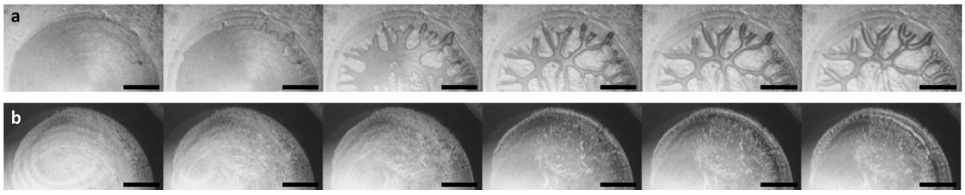

Figure 6. Fingering and cavitation occurring during tack probe retreat on the copolymer films. Images taken every 200 ms during probe retreat at 50 μm·s^{-1} on: a) smooth P*n*BA-*b*-PS film; b) P*n*BA-*b*-PS porous film. Scale bars: 2 mm.

of the sample. The camera resolution does not allow to evidence if micron-sized cavities are generated. However, a melt heterogeneity is growing in the central part during probe retreat. The substrate porosity tends to break down the radially convergent melt flow in favor of an internal one.

4. Discussion

The microscopy images confirmed that PS homopolymer produces highly ordered HC films with small and narrowly distributed pores. On the other hand, the use of the P*n*BA-*b*-PS block copolymer allows to tune surface chemistry while maintaining mechanical strength of BF substrate thanks to the microphase separation. Nevertheless, erratically and broadly distributed large pores are obtained in a large proportion of the porous P*n*BA-*b*-PS block copolymer film. CA and probe tack results show that the chemical nature of smooth substrates presents a minor impact on wetting and adhesion compared to the introduction of the micrometer porosity. It is expected that the substrate porosity influences the polymer melt interface, particularly its insertion in the pores. Without applied pressure, CA analysis completed by the contact line dynamics indicates that the melt spreads easily and fills a significant fraction of the broadly distributed pores from the P*n*BA-*b*-PS copolymer porous film, about 12.5% of the total surface. This process might be also favored by a better affinity between the copolymer and the melt. On the other hand, melt barely gets into the narrowly distributed small pores from the PS HC film. Under an applied pressure, during the initial phase of the tack measurements, the polymer melt is partially pushed into the pores, as demonstrated by the initial probe positions h_0, which significantly decrease for the porous BF substrates. Under these conditions, the precise fraction of empty pores cannot be evaluated. However, probe tack experiment and in-situ optical microscopy are indicative of the presence of empty pores under the melt. The probe tack curves (Figure 5) indicate a pronounced fingering regime on smooth PS films and a cavitation regime (force plateau) on the PS HC film. This well-marked cavitation behavior suggests the presence of several empty pores. Also, images collected on smooth P*n*BA-*b*-PS copolymer film show preeminent fingering, whereas the corresponding porous film texture induces greater melt heterogeneity during probe retraction, which is associated with restricted fingering at the edge of the sample (Figure 6). This reduced lateral expansion of the fingering could be due to partial pinning of the melt by empty smaller pores. However, the number of those empty pores is not sufficient to generate observable cavitation behaviors during probe tack measurements.

5. Conclusion

The versatile breath figure process produces porous films with two surface natures and two pore size distributions: narrowly distributed small pores for PS homopolymer or broadly distributed larger ones for P*n*BA-*b*-PS diblock copolymer. Wetting and adhesion data collected with the low molar mass P*n*BA polymer melt demonstrate the feasibility of performing such measurements without damaging the fragile polymeric BF substrates and illustrate the preeminent influence of the surface pore size distribution. Static C measurements show that both types of porosity enhance the repellency of the polymer melt, while droplet spreading is significantly accelerated by the presence of larger pores. Different tack regimes are observed and correlated with the surface structure: smooth films lead to fingering regimes, whereas the BF-textured films show signatures of cavitation. The correlation between the wetting and adhesion data highlights the major role of melt intrusion into the pores, which can be controlled mainly through the pore dimensions of the polymer film but also through its chemical nature. All these observations show up the role of the pore's size distribution, especially the presence of small ones (i.e., about 2 μm), on the generation of cavities and their impact on decreasing fingering expansion and crack propagation, which is of interest for applications. Further works are still necessary to fully depict adhesion and wetting mechanisms on BF films, such as localizing the polymer melt within the pores, vary melt viscosity, and tune independently interfacial chemistry, substrate mechanical stability, and importantly pore dimension.

Supporting Information

Supporting Information is available from the Wiley Online Library or from the author.

Acknowledgements

The authors thank F. Nallet and P. Fabre at Centre de Recherche Paul Pascal (CRPP) for providing the tack setup. Leon Brillouin Laboratory at CEA-Saclay (LLB) provided neutron beamtime on the PAXY beamline, with the technical support of A. Lapp. SAXS experiments were performed on beamline ID02 at the European Synchrotron Radiation Facility (ESRF), Grenoble, France. The authors are grateful to M. Fernandez at the ESRF for providing assistance in using beamline ID02. Région Aquitaine funded the PhD grant for P.E.

Conflict of Interest

The authors declare no conflict of interest.

Data Availability Statement

The data that support the findings of this study are available from the corresponding author upon reasonable request.

Keywords

adhesion, breath figure templating, wetting

Received: July 29, 2022
Revised: October 19, 2022
Published online: November 11, 2022

[1] G. Widawski, M. Rawiso, B. François, *Nature* **1994**, *369*, 387.
[2] U. H. F. Bunz, *Adv. Mater.* **2006**, *18*, 973.
[3] M. Hernández-Guerrero, M. H. Stenzel, *Polym. Chem.* **2012**, *3*, 563.
[4] M. H. Stenzel, C. Barner-Kowollik, T. P. Davis, *J. Polym. Sci. Pol. Chem.* **2006**, *44*, 2363.
[5] P. Escale, L. Rubatat, L. Billon, M. Save, *Eur. Polym. J.* **2012**, *44*, 9.
[6] A. Muñoz-Bonilla, M. Fernández-García, J. Rodríguez-Hernández, *Prog. Polym. Sci.* **2014**, *39*, 510.
[7] H. Iwanaga, K. Shiratsuchi, H. Yamazaki, *Fujifilm Res. Dev.* **2009**, *54*, 43.
[8] H. Yamazaki, K. Ito, H. Yabu, M. Shimomura, *Soft Matter* **2014**, *10*, 2741.
[9] C. Huang, T. Kamra, S. Chaudhary, X. Shen, *ACS Appl. Mater. Interfaces* **2014**, *6*, 5971.
[10] B. François, O. Pitois, J. François, *Adv. Mater.* **1995**, *7*, 1041.
[11] P. Escalé, L. Rubatat, C. Derail, M. Save, L. Billon, *Macromol. Rapid Commun.* **2011**, *32*, 1072.
[12] P. Escalé, M. Save, A. Lapp, L. Rubatat, L. Billon, *Soft Matter* **2010**, *6*, 3202.
[13] P. Escalé, M. Save, L. Billon, J. Ruokolainen, L. Rubatat, *Soft Matter* **2016**, *12*, 790.
[14] E. Ji, V. Pellerin, F. Ehrenfeld, A. Laffore, A. Bousquet, L. Billon, *Chem. Commun. (Camb.)* **2017**, *53*, 1876.
[15] A. Aynard, L. Pessoni, L. Billon, *Polymer* **2020**, *210*, 123047.
[16] H. Yabu, Y. Matsuo, T. Yamada, H. Maeda, J. Matsui, *Chem. Mater.* **2020**, *32*, 10176.
[17] S. Chen, M.-H. Alves, M. Save, L. Billon, *Polym. Chem.* **2014**, *5*, 5310.
[18] A. Bertrand, A. Bousquet, C. Lartigau-Dagron, L. Billon, *Chem. Commun. (Camb.)* **2016**, *52*, 9562.
[19] P. Marcasuzaa, S. Pearson, K. Bosson, L. Pessoni, J.-C. Dupin, L. Billon, *Chem. Commun. (Camb.)* **2018**, *54*, 13068.
[20] P. Escale, W. Van Camp, F. Du Prez, L. Rubatat, L. Billon, M. Save, *Polym. Chem.* **2013**, *4*, 4710.
[21] P. Marcasuzaa, H. Yin, Y. Feng, L. Billon, *Polym. Chem.* **2019**, *10*, 3751.
[22] H. Yin, A.-L. Bulteau, Y. Feng, L. Billon, *Adv. Mater. Interfaces* **2016**, *3*.
[23] T. Kawano, M. Sato, H. Yabu, M. Shimomura, *Biomater. Sci.* **2014**, *2*, 52.
[24] S. Chen, X. Lu, Y. Hu, Q. Lu, *Biomater. Sci.* **2015**, *3*, 85.
[25] K. Oku, K. Ohno, D. Miyamoto, K. Ito, H. Yabu, K. Nakazawa, *Macromol. Biosci.* **2021**, *21*, 2100113.
[26] A. S. De León, J. Rodríguez-Hernández, A. L. Cortajarena, *Biomaterials* **2013**, *34*, 1453.
[27] S. Falak, B. K. Shin, H. Yabu, D. S. Huh, *Polymer* **2022**, *244*, 124646.
[28] K. Mukai, M. Hara, H. Yabu, S. Nagano, T. Seki, *Adv. Mater. Interfaces* **2021**, *8*, 2100891.
[29] X. Yu, Q.i-Z. Zhong, H.-C. Yang, L.-S. Wan, Z.-K. Xu, *J. Phys. Chem. C* **2015**, *119*, 3667.
[30] Z. Li, X. Ma, D. Zang, Q. Hong, X. Guan, *RSC Adv.* **2015**, *5*, 21084.
[31] Z. Li, Z. Zhang, Q. Kong, X. Ren, *J. Appl. Polym. Sci.* **2017**, *134*.
[32] L. Heng, X. Meng, B. Wang, L. Jiang, *Langmuir* **2013**, *29*, 9491.
[33] H. Yabu, M. Shimomura, *Langmuir* **2005**, *21*, 1709.
[34] H. Yabu, M. Takebayashi, M. Tanaka, M. Shimomura, *Langmuir* **2005**, *21*, 3235.
[35] T. Verho, C. Bower, P. Andrew, S. Franssila, O. Ikkala, R. H. A. Ras, *Adv. Mater.* **2010**, 673.
[36] B. Bhushan, Y. C. Jung, *Prog. Mater. Sci.* **2011**, *56*, 1.
[37] M. Kamperman, E. Kroner, A. Del Campo, R. M. Mcmeeking, E. Arzt, *Adv. Eng. Mater.* **2010**, *12*, 335.
[38] M. Lamblet, E. Verneuil, T. Vilmin, A. Buguin, P. Silberzan, L. Léger, *Langmuir* **2007**, *23*, 6966.
[39] T. Thomas, A. J. Crosby, *J. Adhes.* **2006**, *82*, 311.
[40] C. Poulard, F. Restagno, R. Weil, L. Léger, *Soft Matter* **2011**, *7*, 2543.
[41] L. Dies, F. Restagno, R. Weil, L. Léger, C. Poulard, *Eur. Phys. J. E. Soft Matter* **2015**, *38*, 130.
[42] C. Derail, A. Allal, G. Marin, P. Tordjeman, *J. Adhes.* **1997**, *61*, 123.
[43] C. Derail, A. Allal, G. Marin, P. Tordjeman, *J. Adhes.* **1998**, *68*, 203.
[44] J. Renvoise, D. Burlot, G. Marin, C. Derail, *Int. J. Pharm.* **2009**, *368*, 83.
[45] R. H. Plaut, *J. Adhes.* **2010**, *86*, 1086.
[46] M. Lamblet, "modulation d'adhesion aux interfaces polydimethylsiloxane–adhesif acrylique", in *Physique des Liquides*, Université Paris VI, Paris, **2005**.
[47] H. Lakrout, P. Sergot, C. Creton, *J. Adhes.* **1999**, *69*, 307.
[48] K. R. Shull, C. Creton, *J. Polym. Sci., Part B: Polym. Phys.* **2004**, *42*, 4023.
[49] D. Martina, C. Creton, P. Damman, M. Jeusette, A. Lindner, *Soft Matter* **2012**, *8*, 5350.
[50] C. Creton, M. Ciccotti, *Rep. Prog. Phys.* **2016**, *79*, 046601.
[51] C. Creton, H. Lakrout, *J. Polym. Sci., Part B: Polym. Phys.* **2000**, *38*, 965.
[52] S. Poivet, F. Nallet, C. Gay, J. Teisseire, P. Fabre, *Eur. Phys. J. E. Soft Matter* **2004**, *15*, 97.
[53] S. Poivet, F. Nallet, C. Gay, P. Fabre, *Europhys. Lett.* **2003**, *62*, 244.
[54] P. K. Jha, M. S. Tirumkudulu, *Phys. Fluids* **2007**, *19*, 1.
[55] A. Chiche, P. Pareige, C. Creton, *Comptes Rendus de l'Académie Des Sciences – Series IV – Physics* **2000**, *1*, 1197.
[56] T. Guo, M. Li, L. Heng, L. Jiang, *RSC Adv.* **2015**, *5*, 62078.
[57] N. Jullian, F. Leonardi, B. Grassl, J. Peyrelasse, C. Derail, *Appl. Rheol.* **2010**, *20*, 1.
[58] C. A. Schneider, W. S. Rasband, K. W. Eliceiri, *Nat. Methods* **2012**, *9*, 671.
[59] A. Lafuma, D. Quéré, *Nat. Mater.* **2003**, *2*, 457.
[60] B. Chen, T. Wada, H. Yabu, *Adv. Mater. Interfaces* **2022**, *9*, 2101954.
[61] C. Ishino, K. Okumura, *Eur. Phys. J. E. Soft Matter* **2008**, *25*, 415.
[62] E. Bormashenko, R. Pogreb, G. Whyman, Y. Bormashenko, M. Erlich, *Appl. Phys. Lett.* **2007**, *90*, 201917.
[63] E. Bormashenko, *Colloids Surf. A* **2008**, *324*, 47.
[64] D. Wang, Y. Jiang, Z. Zhu, W. Yin, K. Asawa, C.-H. Choi, J. W. Drelich, *Langmuir* **2020**, *36*, 2622.